Temperature-Dependent Structural and Morphological Engineering of Nickel Nitride via Nitrogen Plasma Processing for Efficient Electrocatalysis

Bo Ouyang[a,c,#], Changhao Deng[a,#], Jinpeng Song[a,#], Yuechuan Du[a], Zheng Zhang[b], Erjun Kan[a,*], Rajdeep Singh Rawat[c,*]

[a] MIIT Key Laboratory of Semiconductor Microstructure and Quantum Sensing, School of Science, Nanjing University of Science and Technology, Nanjing 210094, China
[b] Institute of Materials Research and Engineering, A*STAR (Agency for Science, Technology and Research), #08-03, Fusionopolis Way, Innovis, 138634, Singapore
[c] Natural Sciences and Science Education, National Institute of Education, Nanyang Technological University, 637616, Singapore

[#] These authors contribute equally to this work.

* First corresponding authors:
ekan@njust.edu.cn (Erjun Kan)
rajdeep.rawat@nie.edu.sg (Rajdeep Singh Rawat)

Abstract

Plasma-based surface modulation has gained attention in preparing electrode material for high performance electrocatalysis, but most methods involve multiple steps, typically wet chemical synthesis followed by plasma treatment, limiting further scalability. Solely plasma-driven surface structure control of electrocatalyst remains challenging due to unclear dynamic factors during the plasma discharge, beyond the known values of initial set of plasma discharge parameters. Herein, we develop a cooling-mediated plasma strategy, enabling one-step modulation of structure/phase of the metal electrocatalyst directly on its surface. With nickel as the substrate, controlled surface thermal field during the nitrogen plasma processing yields distinct morphology and facet exposure of the resultant nitrides, attributed to differential distribution of reactive N-species and varied surface dynamics of Ni, verified by in-situ plasma diagnostics and numerical simulations. Based on electrocatalytic performance testing and density functional theory (DFT) simulations, plasma-tailored nano-structures, under controlled surface temperature of electrocatalyst through the use of cooling component, deliver improved hydrogen evolution reaction (HER) and oxygen evolution reaction (OER) activities. Our strategy offers a cost-effective approach for structural engineering in electrocatalysis.

Keywords: Surface structure modulation; Cooling-mediated plasma; Nickel nitride; Electrocatalysis

Introduction

Precise structural modulation is widely recognized as a pivotal strategy for engineering the surface properties of nano-frameworks, especially in the field of electrocatalysis [1, 2]. Among various materials, transition metal nitrides (TMNs) have attracted considerable interest due to their tunable phases and promising functional properties [3, 4]. Numerous methods have been developed for the fabrication of TMNs, with plasma nitridation standing out owing to its rapid processing duration, in-situ nitridation capability and minimal contamination risk [5, 6]. To date, diverse TMNs with tailored structures and morphologies have been successfully fabricated and most strategies rely on the initial growth of oxide precursors followed by plasma nitridation [7, 8]. Although such approaches yield well-defined nitride architectures, the inherently weak interface between the substrate and the grown oxide layer often leads to structural degradation and pulverization during plasma treatment. Additionally, O-based species desorbed from the oxide precursors inevitably introduce undesirable contamination during plasma-substrate interaction. To address such limitations, direct in-situ nitridation of the metallic substrate has emerged as a robust and contamination-resistant strategy for fabrication of high-performance TMN-based catalysts.

During nitrogen plasma processing, reactive N-species present in nitrogen plasma continuously interact with metallic surface, enabling atomic N to diffuse into the metal lattice and form nitride phases [9, 10]. Such approach is able to deliver nitride film and nano-coral frameworks, later of which have garnered increased attentions owing to high structural stability, enlarged surface areas and promising electrocatalytic performance [11]. However, by merely adjusting the initial plasma discharge conditions, conventional plasma processing remains limited in precisely regulating the nitride structure on the metal substrate surface. Although the surface morphology can be adjusted, it remains difficult to selectively control the exposed facets, which restricts the optimization of catalytic properties. In our prior work, a cooling-mediated plasma strategy was demonstrated to regulate the surface thermal field, enabling a transition in exposed facets from thermally stabilized Ni_3N (2-11) phase to the catalytically active Ni_3N (2-10) phase [12]. However, it remains ambiguous whether other facets are to be selectively exposed solely by controlling surface thermal field.

Herein, we further employ the cooling-mediated plasma strategy to modulate the nickel nitride structure directly on Ni surface to achieve other possible surface facets. By maintaining the surface thermal field below 100 °C, the resulting nitride exhibits little nano-coralline structure with exposed facets of Ni_3N (002) and Ni (200). In contrast, conventional plasma processing without any cooling delivers increased surface thermal field up to 130°, leading to well-defined nano-corals with predominantly exposed facet of Ni_3N (101). Such distinct variation arises from the differential distribution of reactive N-species and varied surface dynamics of Ni, as confirmed by in-situ plasma diagnostics and numerical simulations. Electrocatalytic performance evaluation and computational simulations elucidate the electrocatalytic advantages of the resultant nitride nanostructures via different plasma strategies, particularly in enhancing both hydrogen evolution reaction (HER) and oxygen evolution reaction (OER) activities. Such facile plasma processing strategy with controlled surface temperature through the use of substrate cooling module offers a promising pathway for precise structural modulation of metal nitrides with improved electrocatalytic performance.

Experimental Section

2.1. Materials.

Ni plates with the thickness of 0.2 mm were directly purchased from Changsha Lyrun Material Co. Ltd. KOH electrolyte (1 M), HCl solution (3 M) and ethanol (99% purity) have been directly purchased from Changsha Lyrun Material Co. Ltd without further purification.

2.2. Material fabrication

Fabrication of Nickel Nitride Nano-Frameworks (NiNF) via Cooling-Mediated Plasma Processing. The NiNF was fabricated using a custom-designed radio frequency (RF) plasma system integrated with a self-engineered surface thermal field control module [13]. Prior to processing, Ni plates were ultrasonically cleaned in acetone and 3 M HCl solution for 15 min each, followed by thorough rinsing with deionized water and ethanol. The cleaned Ni plates were then positioned inside the plasma chamber, maintaining the 40 cm gap between the capacitively coupled RF electrodes. After evacuating the chamber using the rotary and turbo pump setup, N_2 gas was introduced at a controlled flow rate, and the chamber pressure was stabilized at ~40 Pa using mechanical valves. N_2 plasma was generated via RF power supply

(Caeser136 RF generator) coupled by a Navio matching network. Concurrently, the surface thermal field control system was activated to limit the substrate temperature increase. After 300 s nitridation, the plasma was turned off, and the chamber was vented to atmospheric pressure once the system returned to room temperature. Such resultant sample is denoted as NiNF.

Fabrication of Nickel Nitride Nano-Coral via Conventional Plasma Processing (NiNC). The fabrication of NiNC was conducted following a similar protocol to that for NiNF (same RF power and background pressure), with the absence of surface thermal field regulation. Specifically, during plasma treatment, the surface thermal field control component was deactivated, allowing the substrate temperature to increase continuously throughout the 300 s nitridation process. Such thermal condition facilitates the nano-coral formation of NiNC.

2.2. Characterization, performance evaluation and computational analysis

Characterization: Scanning electron microscopy (SEM) and corresponding energy dispersive X-ray spectroscopy (EDX) were conducted using JEOL JSM-7600F scanning electron microscope at 15 kV. Transmission electron microscopy (TEM) imaging was performed on JEOL-2100F high-resolution transmission electron microscope with an accelerating voltage of 200 kV. X-ray diffraction (XRD) measurements were carried out using Bruker D8 advance diffractometer with Cu Kα radiation ($\lambda = 0.15406$ nm). X-ray photoelectron spectroscopy (XPS) analysis was conducted on VG ESCALAB 220i-XL XPS system equipped with a monochromatic Al Kα (1486.7 eV) X-ray source. The C 1s peak at 284.5 eV, corresponding to sp^2-hybridized carbon, was used for binding energy calibration.

HER Performance Evaluation: The electrochemical measurements were conducted using a CHI 660E electrochemical workstation (CH Instruments) in a three-electrode configuration. Alkaline (1 M KOH) electrolyte was used for testing. The 85% iR-compensation is automatically proceeded during electrocatalytic evaluations. For HER process, saturated calomel electrode (SCE) served as the reference electrode, while the graphite rod and platinum electrodes were used as the counter electrode for HER and OER processes respectively. All prepared catalysts were directly employed as working electrodes without the addition of binders or conductive agents. Cyclic voltammetry (CV), linear sweep voltammetry (LSV), and

electrochemical impedance spectroscopy (EIS) were performed to evaluate the electrocatalytic behaviors and performance of plasma-nitrided samples (NiNF and NiNC). The potential conversion from SCE to reversible hydrogen electrode (RHE) was calculated suing the equation: $E_{RHE} = E_{SCE} + 0.0592 \times pH + 0.242$ (V).

Density Functional Theory (DFT) Computational Analysis: For model construction, the cubic Ni (a=b=c=3.48 Å, α=β=γ=90°) and hexagonal Ni_3N (a=b=4.58 Å, c=4.23 Å, α=β=90°, γ=120°) were applied as the bulk structure. The surface formation energy (ΔE_{SF}) of different facets in Ni_3N was calculated using Vienna Ab-initio Software Package (VASP) with the Perdew-Burke-Emzerhof (PBE) exchange-correlation functional. Based on experimental results, Ni_3N models with typical surfaces were employed. The vacuum layer of 20 Å was introduced along the c-axis of the slab model to eliminate interactions between periodic surfaces. The plane-wave energy cutoff was set to 500 eV, with energy and force convergence criteria set to 10^{-5} eV and 10^{-2} eV $Å^{-1}$, respectively. The ΔE_{SF} of different facets were calculated, using the following equations [14, 15]:

$$\Delta E_{SF}(Ni_3N) = \frac{1}{2A}(E_{tot}^{slab} - N_{Ni3N}E_{tot}^{Ni3N} - (N_N - 2N_{Ni})\mu_N)$$

Where E_{tot}^{slab} refers to the total energy of the slab supercell, E_{tot}^{Ni3N} serves as the energy of bulk Ni_3N per formula unit, and A is the surface area. N_N and N_{Ni} are numbers of N and Ni atoms in the slab, so the $(N_N - 2N_{Ni})$ equals to excessive nitrogen beyond stoichiometric Ni_3N units in the slab. μ_N is the chemical potential of nitrogen.

To theoretically investigate the electrocatalytic performance of Ni- and Ni_3N-based facets, the DFT+D3 calculations were conducted via PBE exchange-correlation function. Intermediate adsorbates were placed on substrate surfaces to determine adsorption energy. All other computational parameters were consistent with those employed in the surface energy calculations.

The binding energy of adsorbates on substrate was determined using the equation:

$$E_{ads} = E_{substrate+adsorbate} - (E_{substrate} + E_{adsorbate})$$

where E_{ads} represents the adsorption energy, $E_{substrate+adsorbate}$ denotes the total energy of the catalyst surface with the adsorbate, and $E_{substrate}$ and $E_{adsorbate}$ correspond to the total energies of the catalyst surface and the adsorbate, respectively.

In such work, the Gibbs free energy change (ΔG) of each elementary step was calculated using:

$$\Delta G = \Delta E + \Delta ZPE - T\Delta S$$

Where the ΔE represents the adsorption energy, ΔZPE and ΔS are the changes in zero-point energy and entropy, respectively, and the temperature T is set to 300, 400, 500, 600 K based on different surface thermal fields values observed during the experiments.

Results and Discussion

During the plasma nitridation, the formation of surface structures is jointly governed by the surface thermal field and the density of N-species on substrate surface. Among these factors, the surface thermal field plays a pivotal role in modulating the spatial distribution of N-species on substrate surface. To investigate the influence of the surface thermal field on nitriding behavior, operando plasma diagnostics were employed to gain insights into the surface modification process. As shown by in-situ infrared measurement (Figure 1a), a significant increase in surface temperature is observed from ambient to 132 °C during conventional plasma processing for 300 s. In comparison, the surface thermal field during NiNF fabrication rises modestly (due to use of substrate cooling component) and stabilizes at 66 °C by the end of nitridation process. Such pronounced divergence in thermal profiles during between two fabrication processes is anticipated to lead to distinctly different surface structures.

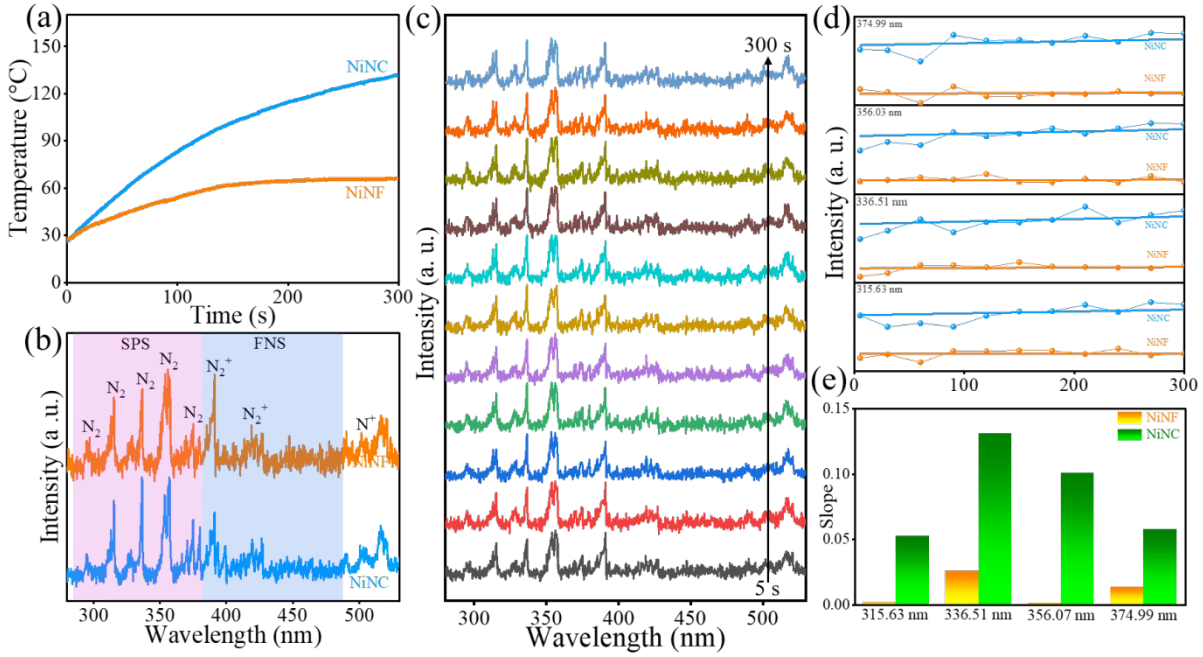

Figure 1. Operando plasma diagnostics during both (with and without cooling component) plasma nitridation process for NiNF and NiNC. (a) The temperature variation of substrate surface, (b) comparison of initial OES spectra, (c) time-dependent OES spectra during NiNF fabrication of 900 s with 20 s interval, (d) typical emission intensity comparison, (e) comparison of the slopes of the linear-fitted key OES peaks' intensity change with time.

The optical emission spectroscopy (OES) spectra at the initial stage for both fabrication processes display distinct emission peaks in the 280-530 nm range (Figure 1b), corresponding to N-species [16, 17]. Accordingly, the plasma environment is identified to contain N_2, N_2^+ and N^+ species. Owing to the presence of plasma sheath on the substrate surface, N_2^+ and N^+ are able to contribute to defect formation on substrate surface. Consequently, their concentration is expected to induce the density difference of surface defects [18]. Additionally, the N serves as the primary source for nitride formation via the diffusion into the substrate [19]. Hence, high surface thermal field enhances the mean free path of reactive N_2^+ and N^+ by extending its mean free path, while simultaneously facilitating the deep penetration of reactive N. In contrast, low surface reaction temperature leads to N-accumulation on substrate surface, resulting in mild penetration and reduced surface etching by N_2^+.

Time-resolved OES measurement further elucidate the influence of the surface thermal field on the emission peaks' intensities of N-species (Figure 1c and Figure S1). Given that the density of N-species is directly proportional to their emission intensity, a comparative analysis reveals a modest increase in emission intensities during the cooling-mediated plasma process.

In comparison, these intensities increase progressively under conventional plasma conditions (Figure 1d), highlighting the dynamic evolution of reactive N-species under varied surface thermal field.

The comparison of slopes derived from the linear fitting of time-resolved emission intensities indicates that the slopes increase progressively during NiNC fabrication (Figure 1e), whereas the slopes remains relatively low during NiNF fabrication process. This observation confirms that conventional plasma processing enhances the density of reactive N-species due to relatively higher and increasing surface reaction temperature for NiNC sample. In contrast, the suppressed thermal field during cooling-mediated plasma processing (NiNF sample) results in the reduced concentration of N-species on substrate surface. The elevated surface temperature promotes the dynamic mobility of surface Ni atoms, while the increased density of reactive N-species facilitates intense interaction with Ni surface. Therefore, it is hypothesized that conventional plasma processing leads to enhanced nitride formation with more pronounced nano-structurization on Ni surface for NiNC sample, as compared to the structures obtained via cooling-mediated plasma for NiNF sample.

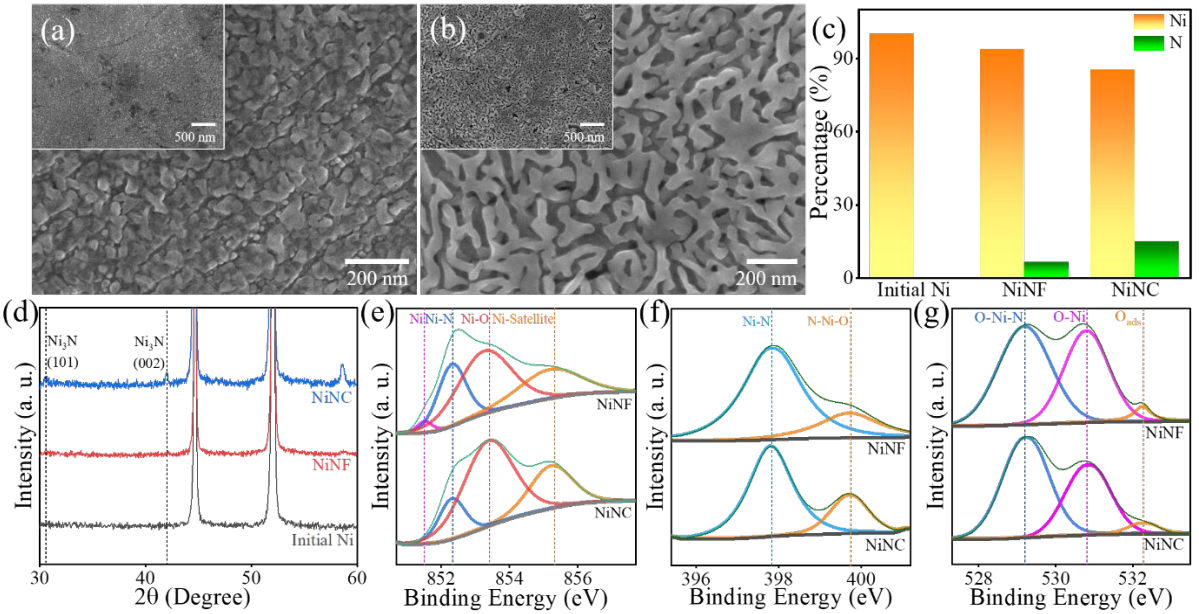

Figure 2. Morphological and structural characterizations of nickel nitrides via plasma processing with (NiNF) and without (NiNC) surface-thermal-field-modulation. SEM images of (a) NiNF and (b) NiNC, (c) atomic percentage of Ni and N via EDX mapping, (d) XRD patterns, XPS analysis of (e) Fe 2p, (f) N 1s, (g) O 1s.

To validate the above hypothesis, comprehensive structural characterizations were

performed. By comparing surface morphology, NiNF exhibits uniformly distributed nano-assemblies (Figure 2a) with the minimal formation of nano-coralline structures. For NiNC, well-defined nano-corals are achieved on Ni surface with the average diameter of 40 nm (Figure 2b). Such morphological difference is attributed to the distinct surface thermal field during NiNF and NiNC samples. For EDX comparison (Figure 2c), increased N-signal is detected on NiNC sample surface, indicating enhanced N-incorporation facilitated by the raised surface thermal field. In terms of XRD analysis (Figure 2d), NiNC presents apparent diffraction peaks at 41.9° and 30.4°, corresponding to (002) and (101) facets of hexagonal Ni_3N [20]. In comparison, NiNF exhibits the Ni_3N (002)-based peaks with the reduced intensity, suggesting a relatively low degree of nitridation, in line with its suppressed surface thermal field. According to XPS Ni 2p spectra (Figure 2e), it is found that both samples deliver the bands at 852.3, 853.4 and 855.3 eV, corresponding to Ni-N, Ni-O and Ni-satellite bands, respectively [21]. However, the binding energy peak band at 851.5 eV, indicative of metallic Ni, is present only in NiNF, suggesting incomplete surface nitridation. For the N 1s (Figure 2f), both samples show the bands at 397.8 and 399.7 eV, attributable to Ni-N and N-Ni-O bonding [22]. Similarly, O 1s spectra display the O-Ni-N, O-Ni and O_{ads} bands at 529.2, 530.8, 532.3 eV (Figure 2g), indicating partial surface oxidation upon exposure to atmospheric conditions, a common phenomenon for most sample surfaces [23].

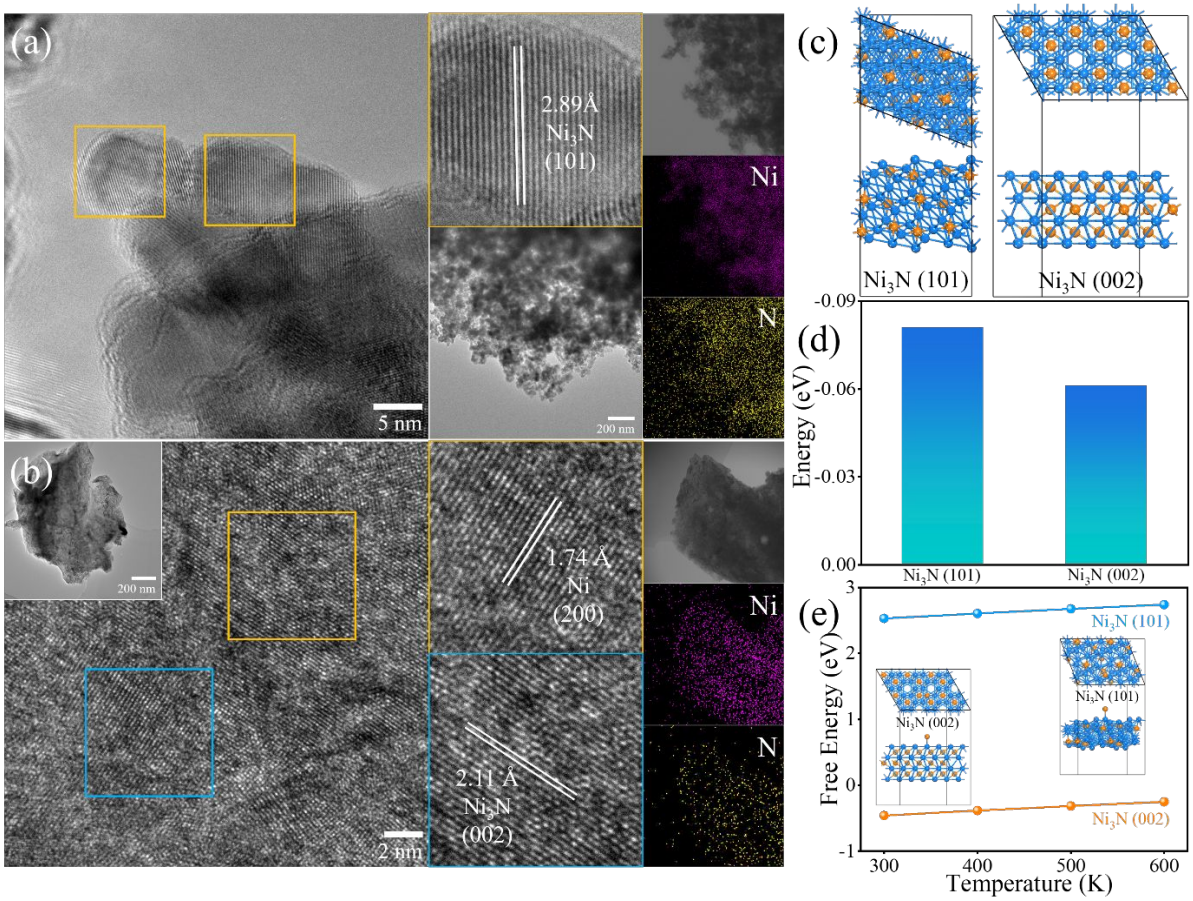

Figure 3. Structural characterizations and simulation analysis of NiNF and NiNC. TEM images of (a) NiNF and (b) NiNC, (c) surface models of Ni_3N (101) and Ni_3N (002), (d) surface formation energy of different facets, (e) and Gibbs free energy for N-adsorption of both facets at different temperature.

TEM analysis reveals distinct structural differences between NiNC and NiNF (Figure 3a-3b). Specifically, NiNC exhibits the Ni_3N (101) facet with the lattice spacing of 2.89 Å. Comparatively, NiNF displays exposed facets of Ni (200) and Ni_3N (002), with the lattice spacings of 1.74 and 2.11 Å, respectively. According to macroscopic TEM observation, NiNC shows nano-coralline morphology, while there are only nano-crystalline frameworks on NiNF, confirming the SEM results. By comparing the TEM-EDX mapping, it is found that the N-species distribution in NiNC is denser compared to NiNF, confirming enhanced N-penetration of NiNC. To further investigate the influence of different plasma nitridation conditions (with and without substrate cooling) on structural evolution and facet exposure, DFT simulation is conducted accordingly. Based on TEM results, surface models of Ni_3N (101) and Ni_3N (002) are constructed (Figure 3c). By comparing ΔE_{SF} of both facets (Figure 3d), Ni_3N (101) exhibits a lower value of -0.08 eV $Å^{-2}$, compared to -0.61 eV $Å^{-2}$ for Ni_3N (002). This indicates that

(101) facet processes the enhanced thermal stability under elevated surface thermal field, in agreement with the experimental observations.

Additionally, during plasma nitridation process, atomic N penetrates the metallic substrate, promoting the nitride formation. Therefore, the Gibbs free energy of N-adsorption (ΔG_{N*}) on the initially formed nitride serves as a crucial indicator of the relative ease of facet formation (Figure 3e). Accordingly, the ΔG_{N*} of Ni_3N (002) is significantly lower than that of Ni_3N (101) facets across the temperature range of 300-600 K. This suggests that N-incorporation is thermodynamically favorable along the Ni_3N (002) facet at elevated temperature. This aligns with the increased intensity of Ni_3N (002) peak in the XRD pattern of NiNC compared to NiNF. Hence, the preferential exposure of Ni_3N (101) facet on the NiNC surface is ascribed to its increased thermal stability, despite its relatively high formation energy. In comparison, the exposure of Ni_3N (002) facet in NiNF is primarily driven by the preferential N-incorporation under the reduced surface thermal field due to the use of cooling component.

The electrochemical evaluation for HER behavior is conducted to investigate the effect of different plasma processing on surface structure evolution. As shown in LSV curves (Figure 4a), the NiNC electrode exhibits the overpotential of 120 and 258 mV at 10 and 50 mA cm^{-2} (J_{10} and J_{50}), respectively. These values are significantly lower than those of NiNF (173 and 310 mV) and initial Ni (206 and 358 mV). Although the Pt electrode delivers a lower overpotential of 60 mV at J_{10}, it shows a higher overpotential at elevated current density, suggesting that the nano-structured surface of NiNC offers abundant accessible active sites which enhance HER kinetics under demanding conditions. To further elucidate the origin of HER activity, electrochemically active surface area (ECSA) measurements are performed, with detailed CV curves presented in Figure S2. As shown in Figure 4b, the NiNC electrode exhibits the double-layer capacitance (C_{dl}) of 2.66 mF cm^{-2}, higher than 2.02 mF cm^{-2} of NiNC. The reduced ECSA in NiNF is mainly attributed to its limited nano-structural formation due to the suppressed surface thermal field. By comparing ECSA normalized LSV curves (Figure S3) of NiNF and NiNC, it can be seen that they exhibit nearly identical catalytic activity. Such result indicates that the per-site catalytic performance of NiNF is comparable to that of NiNC.

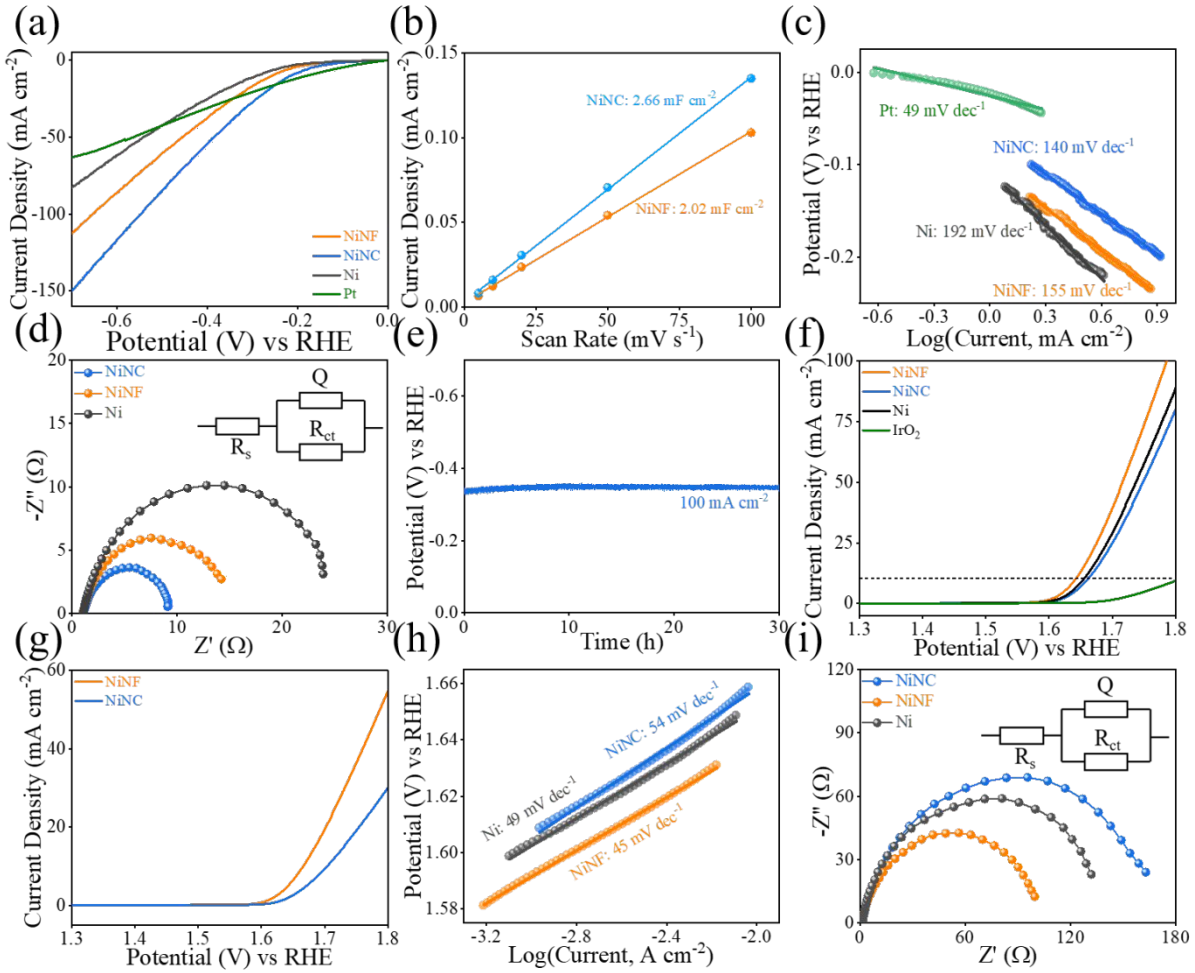

Figure 4. Electrocatalytic behaviors of nickel nitride-based nano-structures via different plasma strategies in alkaline condition. HER behavior of both samples. (a) iR-compensated LSV plots with scan rate of 10 mV s^{-1}, (b) C_{dl} curves, (c) Tafel plots, (d) Nyquist plots, (e) chrono-amperometic profile of NiNC. OER behaviors of both samples. (f) (a) iR-compensated LSV plots with scan rate of 10 mV s^{-1}, (g) Normalized LSV plots by ECSA, (h) Tafel plots, (i) Nyquist plots.

The per-site turnover frequency (TOF), a critical metric for assessing intrinsic electrocatalytic activity, is further analyzed at the overpotential of 0.3 V (Figure S4, detailed methodology provided in Supporting Information). Based on TEM results, Ni_3N (101) is identified as the predominant exposed facet in NiNC, while NiNF presents two active facets, Ni_3N (002) and Ni (200). Therefore, the per-site TOF of NiNF is calculated as the average contribution from both facets. Accordingly, NiNC provides a higher per-site TOF of 3.68 s^{-1} compared to 3.10 s^{-1} of NiNF, highlighting the superior catalytic activity of NiNC. Based on Tafel slope (Figure 4c), NiNC electrode exhibits the slope of 140 mV dec^{-1}, lower than those of NiNF (155 mV dec^{-1}) and initial Ni (192 mV dec^{-1}). The reduced Tafel slope of NiNC suggests favorable reaction kinetics, reinforcing the improved electrocatalytic performance of

the nitride nano-coral via conventional plasma. EIS measurements further corroborate these results (Figure 4d). The charge transfer resistance (R_{ct}) of NiNC is 5.6 Ω, lower than that of NiNF (8.3 Ω) and initial Ni (16.4 Ω), indicating enhanced charge transfer efficiency. Long-term durability testing reveals that NiNC maintains stable catalytic behavior for 30 h at 100 mA cm^{-2}, with negligible degradation (Figure 4e). Additionally, the comparison of LSV curves before and after cycling shows minimal potential change (Figure S5), confirming the great catalytic stability of NiNC in alkaline condition. Based on post-cycling surface characterizations, NiNF electrode exhibit minimal alternations in both morphology and crystal structure, indicating its exceptional structural stability (Figure S6).

In terms of OER performance, LSV curves reveals apparent difference (Figure 4f). The NiNF electrode exhibits a potential of 1.63 V at J_{10}, lower than those of NiNC (1.67 V) and initial Ni (1.65 V). Furthermore, NiNF exhibits an enhanced current density of 40 mA cm^{-2} at 1.7 V, higher than 24, and 28 mA cm^{-2} of NiNC, and initial Ni, respectively. According to EBSA normalized LSV curves (Figure 4g), the NiNF demonstrates improved OER catalytic behavior compared to NiNC, suggesting that the exposed surface structure plays a more critical role in dictating electrocatalytic performance compared to surface area. According to per-site TOF (Figure S6), NiNF exhibits the value of 2.55 s^{-1} at 1.7 V, higher than 1.18 s^{-1} of NiNC. Tafel slope analysis (Figure 4h) reveals the value of 45 mV dec^{-1} for NiNF, lower than those of NiNC (54 mV dec^{-1}) and initial Ni (49 mV dec^{-1}), indicating its improved reaction dynamics. Nyquist plots show that NiNF possesses lower R_{ct} compared to NiNC and Ni_3N (Figure 4i). Long-term stability testing further demonstrates that NiNF maintains stable OER with little activity loss over 10 h at 100 mA cm^{-2} (Figure S7a). The LSV plots before and after durability test shows minimal overpotential increase (Figure S7b). Post-cycling characterizations reveals negligible structural degradation in NiNC electrode, confirming its exceptional structural preservation (Figure S9). In terms of overall water splitting performance, the system based on NiNC and NiNF exhibits the potential of 1.63 V at J_{10} (Figure S10a). Additionally, the prolonged cycling test conducted at J_{10} confirm excellent electrochemical stability (Figure S10b), underscoring the suitability for overall water splitting.

A detailed DFT simulation is performed to support the experimental electrochemical results.

Guided by the structural characterizations, NiNF primarily exposes Ni (200) and Ni_3N (002) facets, whereas NiNC reveals the exposure of Ni_3N (101) facet. To systematically investigate the electrocatalytic behavior of these surfaces, the adsorption behaviors of Ni (200), Ni_3N (002) and Ni_3N (101) surfaces towards relevant intermediates in HER and OER processes are compared (corresponding surface models shown in Figure S8-S10). In these models, surface Ni atoms are designated as the active sites. Given that the HER occurs under alkaline conditions, where the concentration of free H^+ is extremely low, H_2O serves as the main H-source. The reaction follows the pathway: $* \rightarrow H_2O* \rightarrow H*+OH* \rightarrow H* \rightarrow H_2$, which is the reverse of hydrogen oxidation reaction, in line with previously reported mechanism [24]. In terms of Gibbs free energy diagram (Figure 5a), the rate-determining step (RDS) on Ni_3N (101) surface is the dissociation of H_2O from H_2O* to H*+OH*. In contrast, on Ni (200) and Ni_3N (002) surfaces, the RDS is the OH-desorption from H*+OH* to H*. By comparing the RDS of varied surfaces (Figure S11), Ni_3N (101) exhibits the RDS value of 1.14 eV, while Ni_3N (002) and Ni (200) provides the values of 0.93 eV and 1.36 eV, respectively. This indicates that although Ni_3N (002) supports facile OH-desorption, the relatively high energy barrier of Ni (200) adversely affects HER behavior. Thus, the coexistence of these two facets in NiNF leads to a trade-off effect, explaining its relatively lower HER activity compared to NiNC.

For OER process (Figure 5b), the RDS for all surfaces is from HO* to O*. Accordingly, Ni_3N (101) facet exhibits the free energy value of 1.97 eV, whereas Ni_3N (002) and Ni (200) display the values of 1.76 and 1.70 eV, respectively. This highlights the enhanced OER behavior of NiNF compared to NiNC, attributed to the synergistic contribution of Ni_3N (002) and Ni (200) phases. To further understand the facet-dependent catalytic behavior, the partial density of state (PDOS) is analyzed (Figure 5c). The d-band center of the Ni-site on Ni_3N (002) is observed to shift far from Fermi level compared to Ni_3N (101) and Ni (200). This downshift implies the strong anti-bonding interaction between Ni 3d orbitals and adsorbate species, facilitating enhanced catalytic activity [25]. Additionally, the H- and OH-binding energy (HBE and HOBE) are investigated for each facet (Figure 5d). Ni_3N (101) and Ni (002) exhibit higher HOBE values compared to Ni_3N (002), suggesting weaker OH-desorption tendencies and thus reduced HER behavior. Conversely, the Ni_3N (002) facet shows the increased HBE, hindering

H-desorption during HER process.

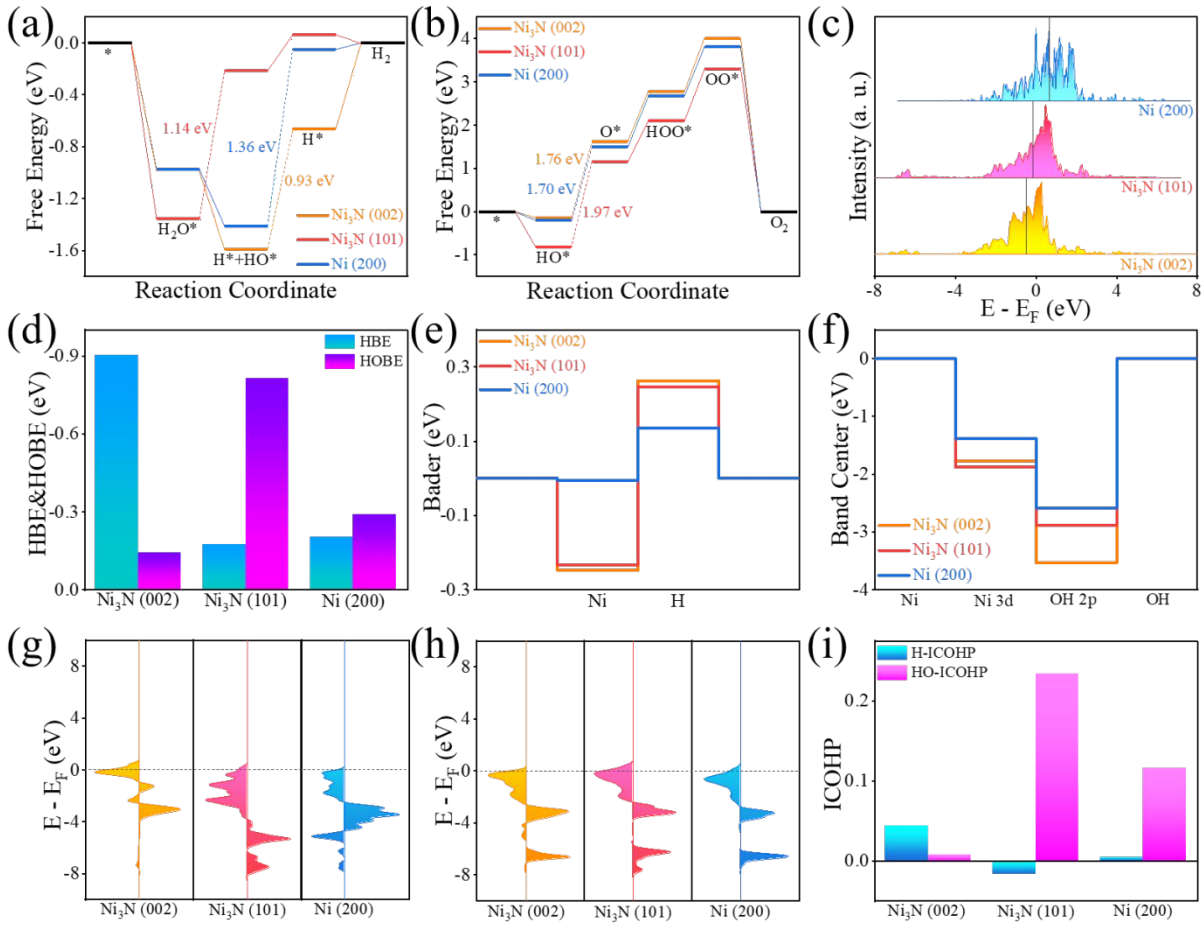

Figure 5. DFT-Simulated HER and OER behaviors of Ni_3N- and Ni-based facets models. Free energy diagrams during (a) HER procedure in alkaline media and (b) OER procedure. (c) d-band center comparison of Ni 3d, (d) HBE and HOBE comparison, (e) Bader charge, (f) d-p band hybridization of Ni-OH bond. COHP comparison of (g) Ni-H and (i) Ni-OH bonds. (i) ICOHP comparison.

Bader charge analysis further supports such results (Figure 5e). Charge transfer between Ni and H on Ni_3N (002) is greater than other facets, with Ni (200) showing the lowest charge transfer. Similarly, the Ni_3N (002) facet exhibits the lowest charge transfer between Ni and OH compared to other facets (Figure S12), consistent with HBE and HOBE trends. Given that all electrochemical performance assessments are conducted in alkaline condition, the 3d-2p orbital hybridization between surface Ni and adsorbed OH is analyzed across different surfaces to further elucidate the catalytic mechanism (Figure 5f). Accordingly, the band center distances between Ni 3d and O 2p on Ni_3N (002) and Ni (200) are higher than that on Ni_3N (101). This indicates the relatively weak hybridization and hence reduced binding energy between Ni and OH. Such weakened binding facilitates OH-desorption, which is crucial for efficient OER

kinetics, thus confirming the enhanced electrocatalytic behavior of NINF.

To further clarify the improved HER and OER activities at the atomic level, crystal orbit Hamiltonian population (COHP) analysis is performed [26]. As illustrated in Figure 5g, the H-COHP analysis reveals that the Ni_3N (002) facet exhibits lower antibonding contribution near the Fermi level compared to Ni_3N (101) and Ni (200), indicating stronger H-adsorption behavior. Regarding OH-adsorption behavior (Figure 5h), HO-COHP analysis shows the apparent down-shift of Ni_3N (002), indicating the increased antibonding proportion compared other facets, and hence the reduced HO-adsorption behavior. The integrated COHP values (ICOHP) in H-ICOHP and OH-ICOHP further corroborates such results (Figure 5i), quantitatively validating the improved HER behavior of NiNC and improved OER behavior of NiNF.

Conclusion

In summary, we have developed a cooling-mediated plasma strategy for direct structural modulation of nickel nitride on Ni substrates. By maintaining the surface thermal field below 100 °C, the synthesized nitride (NiNF) exhibits little nano-coralline structure with exposed facets of Ni_3N (002) and Ni (200). In contrast, conventional plasma processing without any external cooling of substrate delivers raised surface thermal field up to 130°, yielding apparent nano-corals with predominantly exposed facet of Ni_3N (101) in NiNC sample. Such difference stems from the varied densities of reactive N-species, inferenced from varied emission peak intensities in OES, and surface dynamics of atomic N, confirmed by in-situ plasma diagnostics and numerical simulations. Performance evaluation and computational simulations further demonstrate the enhanced HER by NiNC and enhanced OER by NiNF of plasma-tailored nitride nano-structures. Such facile plasma strategy offers a cost-effective pathway for precise structural modulation of metal nitrides towards improved electrocatalytic performance toward specific process, HER or OER.

Declaration of competing interest

The authors declare that they have not known competing financial interests or personal

relationships that could have appeared to influence the work reported in this paper.

Acknowledgement

This study is supported by National Natural Science Foundation of China (12304020), National Science Fund for Distinguished Young Scholars (T2125004), Natural Science Foundation of Jiangsu Province (BK20230909), Fundamental Research Funds for the Central Universities (30923011013, 2025201009), Funding of NJUST (TSXK2022D002), China, and was also supported by NIE AcRF grant RI 7/22 RSR.

References

[1] Y. Deng, S. Xiao, Y. Zheng, X. Rong, M. Bai, Y. Tang, T. Ma, C. Cheng, C. Zhao, Emerging electrocatalytic activities in transition metal selenides: synthesis, electronic modulation, and structure-performance correlations, Chemical Engineering Journal, 451 (2023) 138514.

[2] R. Cheng, Y. Min, H. Li, C. Fu, Electronic structure regulation in the design of low-cost efficient electrocatalysts: From theory to applications, Nano Energy, 115 (2023) 108718.

[3] Y.-Q. Jiao, H.-J. Yan, C.-G. Tian, H.-G. Fu, Structure engineering and electronic modulation of transition metal interstitial compounds for electrocatalytic water splitting, Accounts of Materials Research, 4 (2022) 42-56.

[4] J. Li, S.U. Abbas, H. Wang, Z. Zhang, W. Hu, Recent advances in interface engineering for electrocatalytic CO 2 reduction reaction, Nano-Micro Letters, 13 (2021) 1-35.

[5] H. Wang, J. Li, K. Li, Y. Lin, J. Chen, L. Gao, V. Nicolosi, X. Xiao, J.-M. Lee, Transition metal nitrides for electrochemical energy applications, Chemical Society Reviews, 50 (2021) 1354-1390.

[6] Z. Cheng, W. Qi, C.H. Pang, T. Thomas, T. Wu, S. Liu, M. Yang, Recent advances in transition metal nitride-based materials for photocatalytic applications, Advanced Functional Materials, 31 (2021) 2100553.

[7] Q. Luo, C. Lu, L. Liu, M. Zhu, A review on the synthesis of transition metal nitride nanostructures and their energy related applications, Green Energy & Environment, 8 (2023) 406-437.

[8] Z.-G. Yang, H.-M. Xu, T.-Y. Shuai, Q.-N. Zhan, Z.-J. Zhang, K. Huang, C. Dai, G.-R. Li,

Recent progress in the synthesis of transition metal nitride catalysts and their applications in electrocatalysis, Nanoscale, 15 (2023) 11777-11800.

[9] A. Yetim, H. Kovacı, Y. Uzun, H. Tekdir, A. Çelik, A comprehensive study on the fatigue properties of duplex surface treated Ti6Al4V by plasma nitriding and DLC coating, Surface and Coatings Technology, 458 (2023) 129367.

[10] B. Ouyang, Y. Zhang, Z. Zhang, H.J. Fan, R.S. Rawat, Nitrogen-plasma-activated hierarchical nickel nitride nanocorals for energy applications, Small, 13 (2017) 1604265.

[11] Y. Zhang, B. Ouyang, J. Xu, S. Chen, R.S. Rawat, H.J. Fan, 3D Porous Hierarchical Nickel-Molybdenum Nitrides Synthesized by RF Plasma as Highly Active and Stable Hydrogen-Evolution-Reaction Electrocatalysts, Advanced Energy Materials, 6 (2016).

[12] B. Ouyang, Y. Zhang, X. Wang, Y. Deng, F. Liu, Z. Fang, R.S. Rawat, E. Kan, Facet Control of Nickel Nitride Nano-Framework for Efficient Hydrogen Evolution Electrocatalysis via Auxiliary Cooling Assisted Plasma Engineering, Small, 18 (2022) 2204634.

[13] B. Ouyang, H. Qin, F. Li, C. Li, Z. Du, Y. Zhang, L. Yang, E. Kan, K. Xu, Z. Mi, Phase-tailored CoCrFeNiAl nitride for enhanced electrocatalytic hydrogen evolution via cooling-mediated plasma strategy, Nanoscale, 17 (2025) 10177-10186.

[14] G.H. Chen, Z.F. Hou, X.G. Gong, Structural and electronic properties of cubic HfO2 surfaces, Computational Materials Science, 44 (2008) 46-52.

[15] T.J. Frankcombe, O.M. Løvvik, The Crystal Structure and Surface Energy of NaAlH4: A Comparison of DFT Methodologies, The Journal of Physical Chemistry B, 110 (2006) 622-630.

[16] X.-M. Zhu, Y.-K. Pu, Using OES to determine electron temperature and density in low-pressure nitrogen and argon plasmas, Plasma Sources Science and Technology, 17 (2008) 024002.

[17] J. Kaupe, P. Riedl, D. Coenen, S. Mitic, Temporal evolution of electron density and temperature in low pressure transient Ar/N2 plasmas estimated by optical emission spectroscopy, Plasma Sources Science and Technology, 28 (2019) 065012.

[18] Y. Wang, Y. Yang, H. Yang, M. Zhang, S. Ma, J. Qiao, Microstructure and wear properties of nitrided AlCoCrFeNi high-entropy alloy, Materials Chemistry and Physics, 210 (2018) 233-

239.

[19] T. Moskalioviene, A. Galdikas, J. Rivière, L. Pichon, Modeling of nitrogen penetration in polycrystalline AISI 316L austenitic stainless steel during plasma nitriding, Surface and Coatings Technology, 205 (2011) 3301-3306.

[20] N. Pandey, M. Gupta, J. Stahn, Study of reactively sputtered nickel nitride thin films, Journal of Alloys and Compounds, 851 (2021) 156299.

[21] M. Shalom, D. Ressnig, X. Yang, G. Clavel, T.P. Fellinger, M. Antonietti, Nickel nitride as an efficient electrocatalyst for water splitting, Journal of Materials Chemistry A, 3 (2015) 8171-8177.

[22] S.H. Gage, D.A. Ruddy, S. Pylypenko, R.M. Richards, Deep eutectic solvent approach towards nickel/nickel nitride nanocomposites, Catalysis Today, 306 (2018) 9-15.

[23] B. Ouyang, C. Sun, Y. Du, A. Chaurasiya, Z. Zhang, J. Zhu, E. Kan, F. Li, R.S. Rawat, Operando facet control of hydrophobic iron nitride nano-coral for surface protection via field-modulated plasma strategy, Applied Surface Science, 675 (2024) 160972.

[24] X. Yang, B. Ouyang, L. Zhao, Q. Shen, G. Chen, Y. Sun, C. Li, K. Xu, Ultrathin Rh Nanosheets with Rich Grain Boundaries for Efficient Hydrogen Oxidation Electrocatalysis, Journal of the American Chemical Society, 145 (2023) 27010-27021.

[25] J.-H. Lee, D. Yim, J.H. Park, C.H. Lee, J.-M. Ju, S.U. Lee, J.-H. Kim, Tuning d-band centers by coupling PdO nanoclusters to WO 3 nanosheets to promote the oxygen reduction reaction, Journal of Materials Chemistry A, 8 (2020) 13490-13500.

[26] S. Gu, S. Xu, X. Song, H. Li, Y. Wang, G. Zhou, N. Wang, H. Chang, Electrostatic potential-induced Co–N4 active centers in a 2D conductive metal–organic framework for high-performance lithium–sulfur batteries, ACS Applied Materials & Interfaces, 14 (2022) 50815-50826.

Supporting Information for

Temperature-Dependent Structural and Morphological Engineering of Nickel Nitride via Nitrogen Plasma Processing for Efficient Electrocatalysis

Bo Ouyang[a,c,#], Changhao Deng[a,#], Jinpeng Song[a,#], Yuechuan Du[a], Zheng Zhang[b], Erjun Kan[a,*], Rajdeep Singh Rawat[c,*]

[a] MIIT Key Laboratory of Semiconductor Microstructure and Quantum Sensing, School of Science, Nanjing University of Science and Technology, Nanjing 210094, China
[b] Institute of Materials Research and Engineering, A*STAR (Agency for Science, Technology and Research), #08-03, Fusionopolis Way, Innovis, 138634, Singapore
[c] Natural Sciences and Science Education, National Institute of Education, Nanyang Technological University, 637616, Singapore

[#] These authors contribute equally to this work.

* First corresponding authors:
ekan@njust.edu.cn (Erjun Kan)
rajdeep.rawat@nie.edu.sg (Rajdeep Singh Rawat)

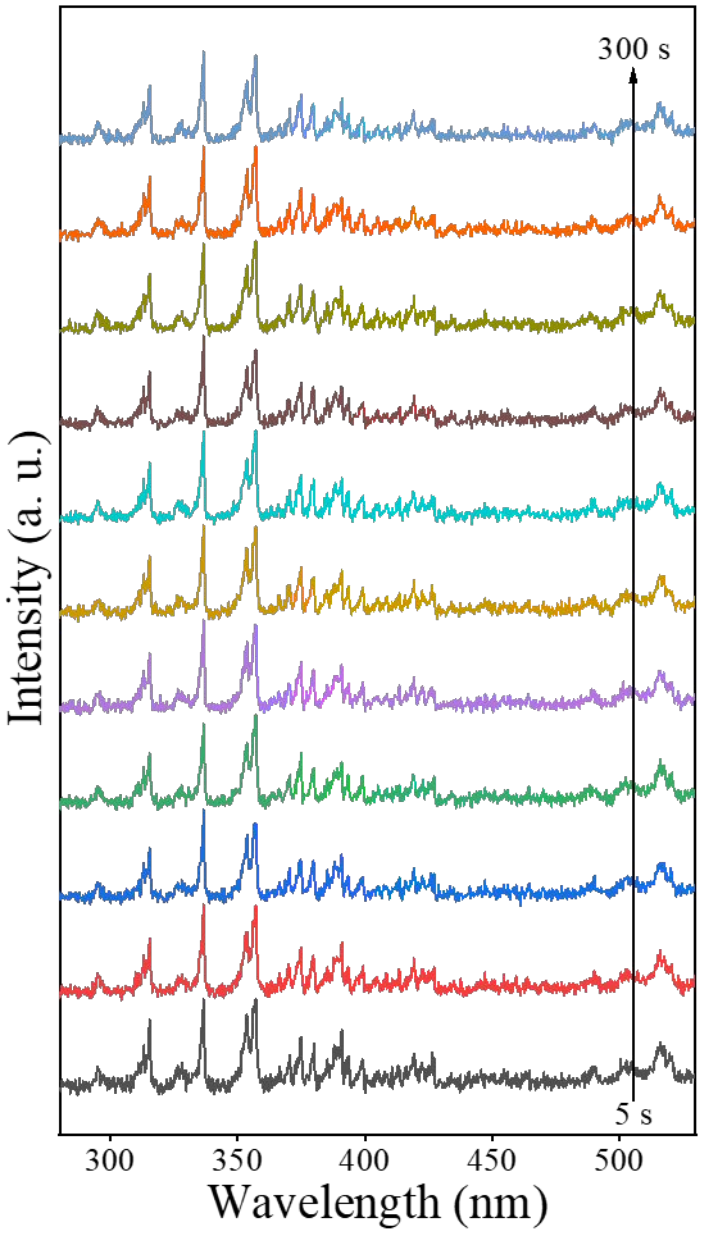

Figure S1. Time-resolved OES spectra during NiNC fabrication.

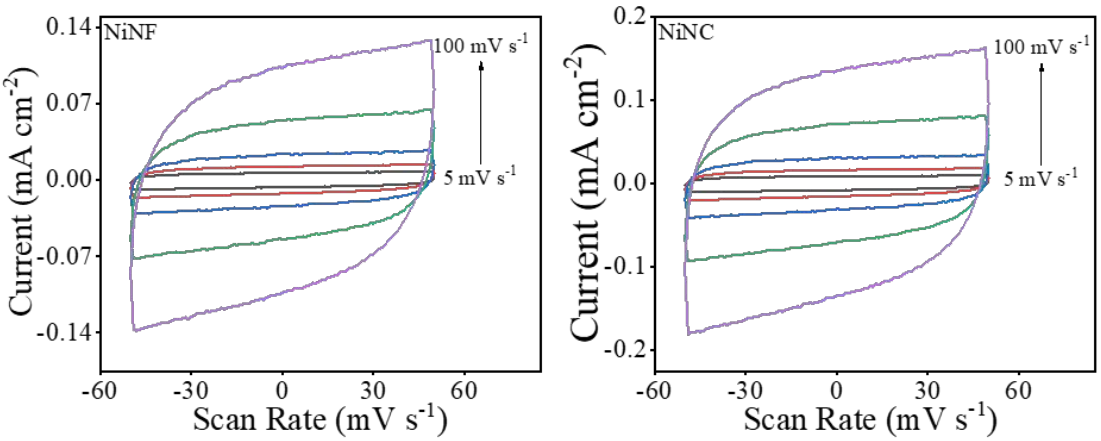

Figure S2. CV curves of different samples within alkaline media.

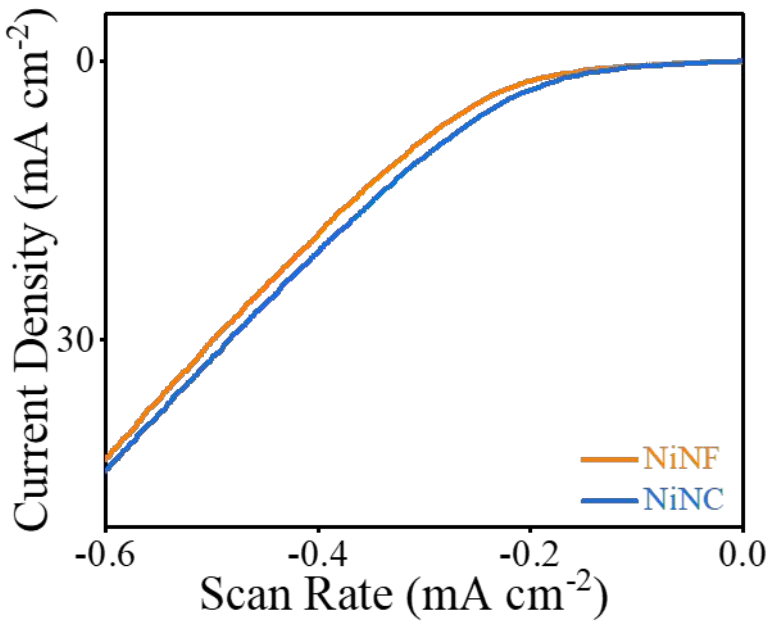

Figure S3. ECSA-normalized LSV profiles of NiNF and NiNC during HER process.

The C_{dl} can be converted to an ECSA using the C_{dl} value for a flat standard with 1 cm^2 of real surface area. The C_{dl} for a flat surface is generally found to be in the range of 20-60 μF cm^{-2}. In the following calculations of turnover frequency (TOF), we assume 40 μF cm^{-2} as a moderate value.

Calculated electrochemical active surface area：

$$A_{ECSA} = C_{dl} / 40\ \mu F\ cm^{-2}$$

To calculate the persite TOF, we apply the following formula:

persite TOF = number of total H_2 turnover of geometric area / number of active sites of geometric area.

The total number of H_2 turnovers can be calculated from the current density according to:

$$\text{Total TOF} = \text{current density} \times 3.12 \times 10^{15}$$

Number of active sites of geometric area can be calculated based on the following formula:

$$\text{Number of active sites} = \text{active site per unit facet} \times A_{ECSA} / \text{area of unit facet}$$

Finally, the plot of current density can be converted into a persite TOF plot based on the above formulas.

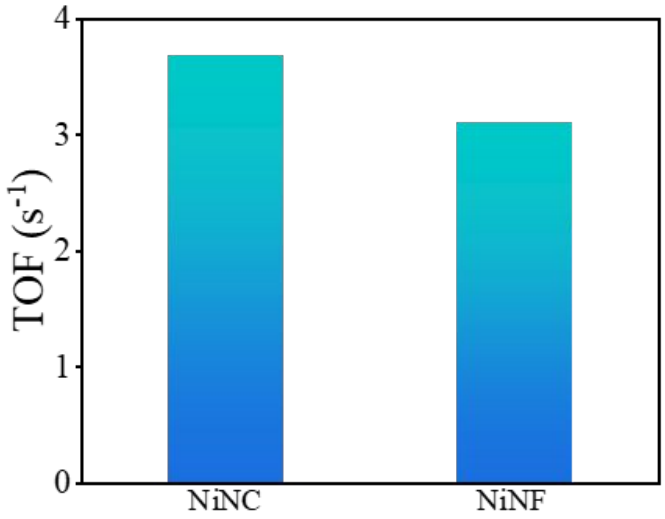

Figure S4. TOF values of NiNC and NiNF during HER process at 0.3 V.

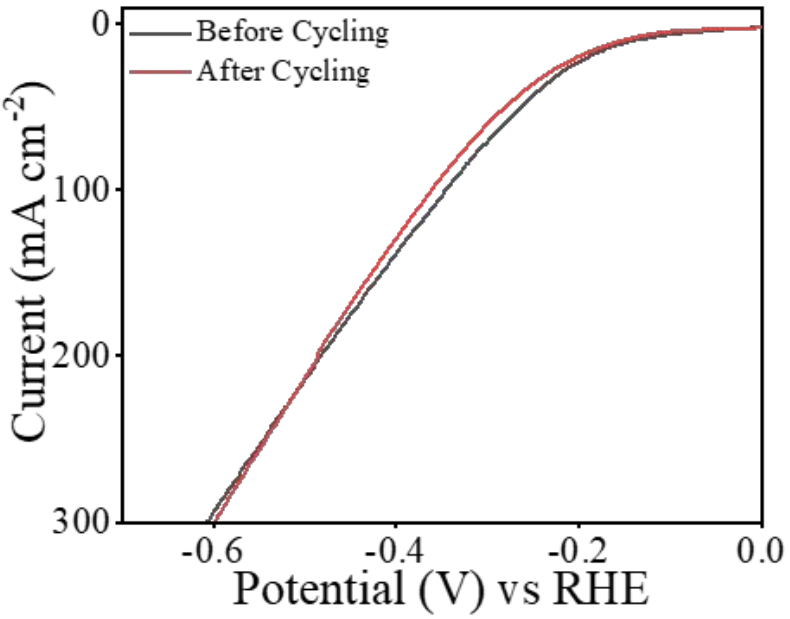

Figure S5. LSV profile of NiNC before and after cycling.

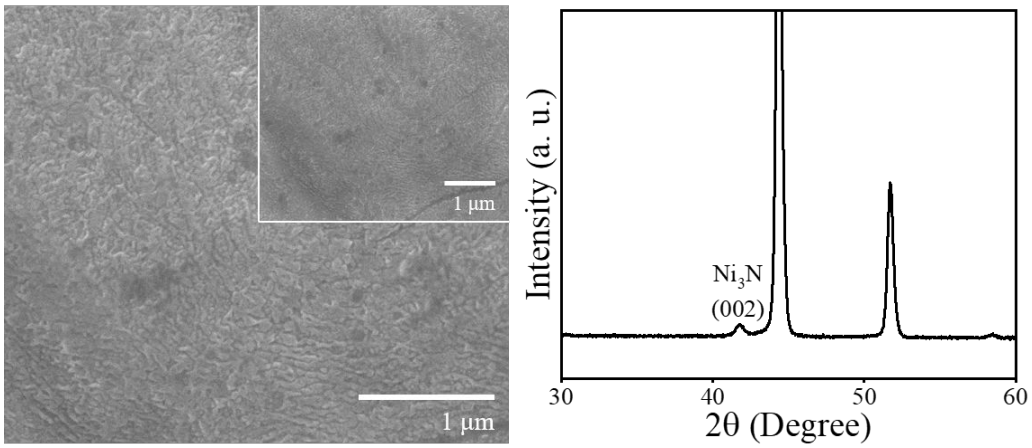

Figure S6. SEM and XRD characterizations of NiNF after cycling.

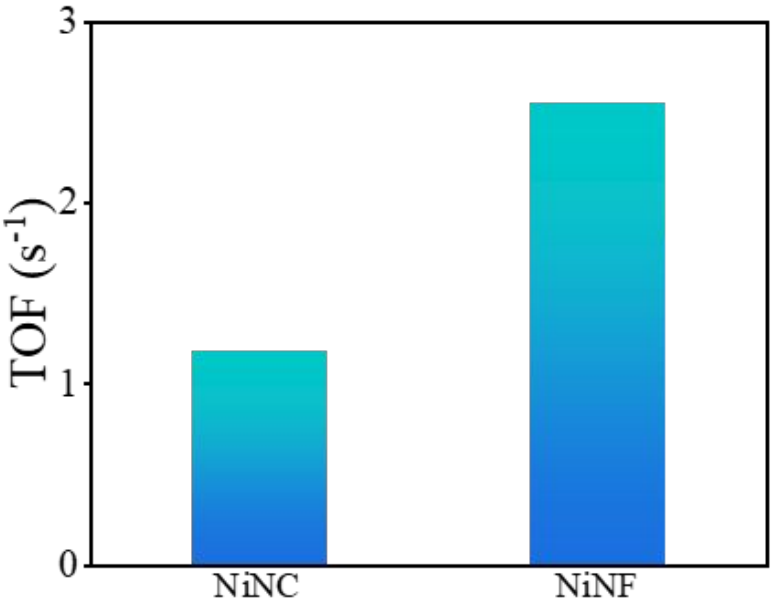

Figure S7. TOF values of NiNC and NiNF during OER process at 1.7 V.

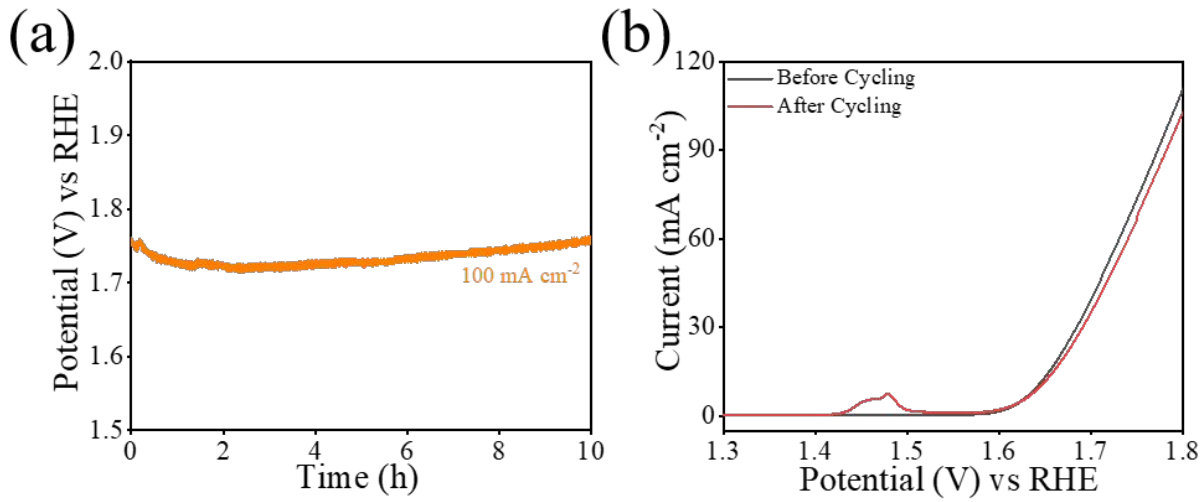

Figure S8. (a) Cycling test of NiNF during OER process, (b) LSV profile of NiNF before and after cycling.

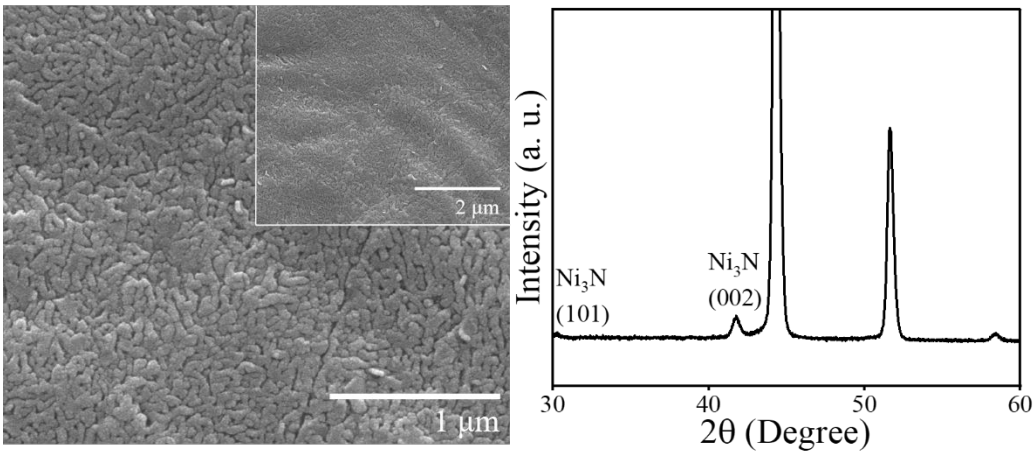

Figure S9. SEM and XRD characterizations of NiNC after cycling.

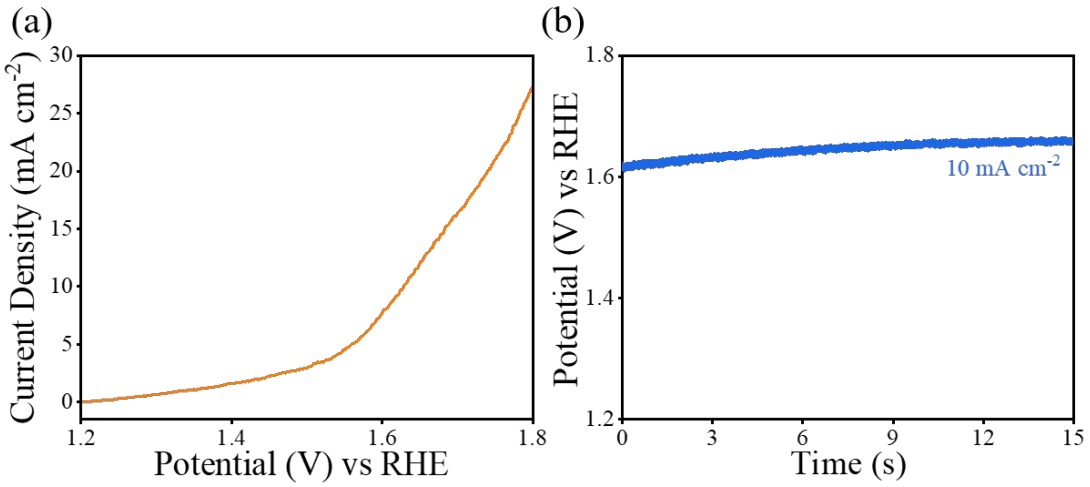

Figure S10. Overall water splitting based on NiNF and NiNC electrodes. (a) LSV curve, (b) cycling process.

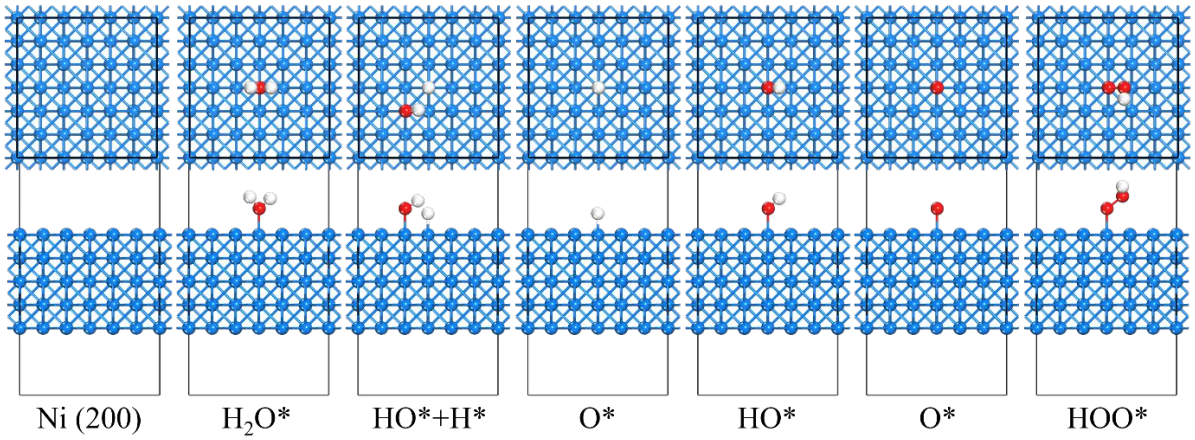

Figure S8. Ni (200) surface model with the adsorption of different species during HER and OER processes.

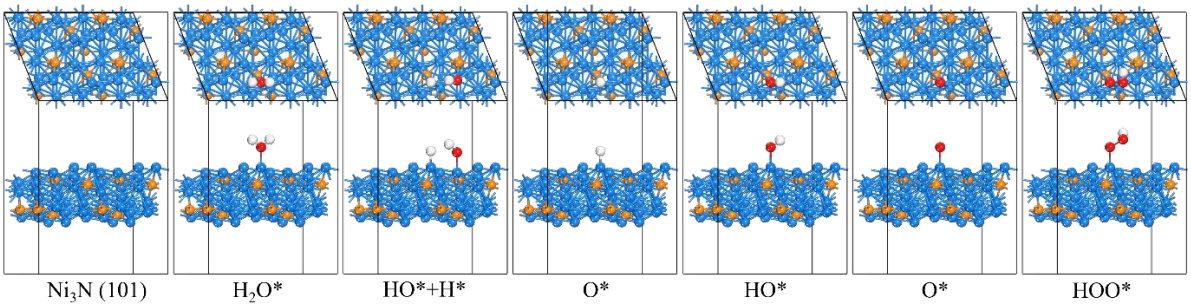

Figure S9. Ni_3N (101) surface model with the adsorption of different species during HER and OER processes.

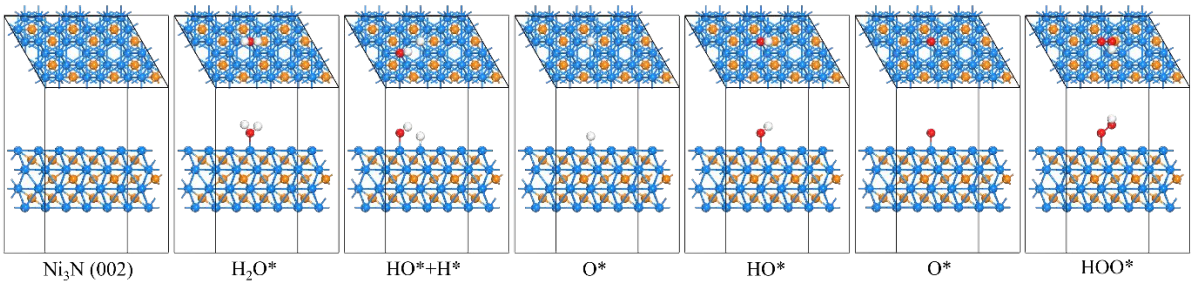

Figure S10. Ni_3N (002) surface model with the adsorption of different species during HER and OER processes.

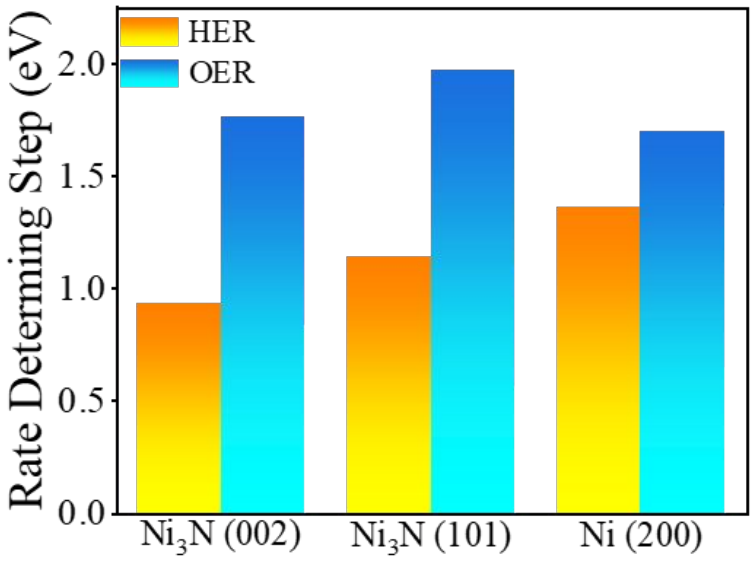

Figure S11. Theorical rate determining step of different surfaces during HER and OER processes

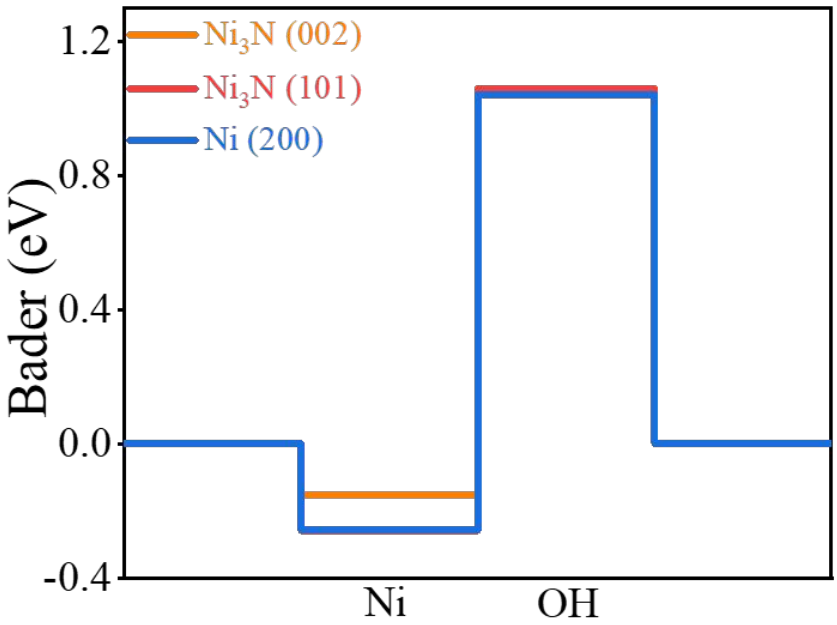

Figure S12. Bader charge of surface Ni and adsorbed OH.

Table of Content

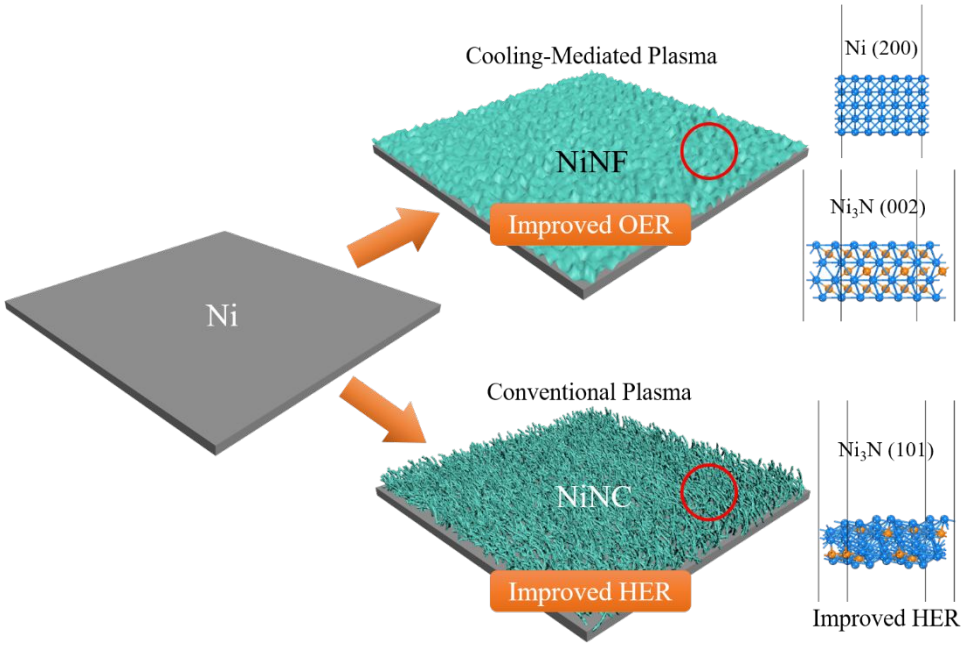

A facile cooling-mediated plasma strategy is applied to simply modulate exposed facets and morphology of the achieved nickel nitride nano-frameworks for controllable HER and OER behaviors.